

## Simulation of the Deformation Mechanisms of Bulk Metallic Glass (BMG) Foam using the Material Point Method

Jin Ma<sup>1</sup>, Jay C. Hanan<sup>1</sup>, Ranga Komanduri<sup>1</sup> and Hongbing Lu<sup>2</sup>

**Abstract:** Amorphous metallic foams are an exciting class of materials for an array of high impact absorption applications, the mechanical behavior of which is only beginning to be characterized. To determine mechanical properties, guide processing, and engineer the microstructure for impact absorption, simulation of the mechanical properties is necessary as experimental determination alone can be expensive and time consuming. In this investigation, the material point method (MPM) with  $C^1$  continuous shape function is used to simulate the response of a bulk metallic glass (BMG) closed-cell foam ( $\text{Pd}_{42.5}\text{Cu}_{30}\text{Ni}_{7.5}\text{P}_{20}$ ) under compression. The BMG foam was also tested experimentally under compression for validation of the simulation results. To build the model for simulation, the complex internal microstructure of the 70% porosity foam was characterized using micro-computed tomography ( $\mu$ -CT). Material points for the simulation, with location and mass density determined from  $\mu$ -CT, were assigned to the cell-walls. The mechanical properties of the cell-walls were determined from nanoindentation and used as inputs for the MPM model. Minimum size of the representative volume element (RVE) used for the simulation of the mechanical response prior to failure was shown to depend on local density. In order to accurately characterize yield of the bulk sample, an RVE must be selected with a dimension of at least 6 average cell diameters. Such an RVE also exhibits bulk sample density. A material point deletion method, using a critical equivalent plastic strain as the failure criterion, was used for simulation of failure in the walls that leads to the collapse of the foam. Simulation of the full densification of an RVE was made to a compressive strain of 80%. Results indicate that prior to full consolidation,  $\sim 50\%$  of cells carry a majority of the load. The load applied on the foam transfers from one region of

---

<sup>1</sup> School of Mechanical and Aerospace Engineering, Oklahoma State University, Stillwater, Oklahoma 74078-5016, USA

<sup>2</sup> Department of Mechanical Engineering, The University of Texas at Dallas, Richardson, Texas 75080-3021, USA. phone: 972-658-5459, fax: 972-883-4659, e-mail: hongbing.lu@utdallas.edu, (H. Lu)

a cell to another, as compression increases. Significant cell-wall bending followed by local buckling is observed, contributing to the collapse of the cell-walls in the foam. While compression induces primarily bending and compressive stresses, the loading path forms diagonally to the loading axis, exhibiting an apparent shear band as the global failure mode.

**Keywords:** Bulk metallic glass (BMG), metal foam, MPM, compression, simulation, nanoindentation, densification, representative volume

## 1 Introduction

Metallic glass is a metastable phase of a metal or its alloy. In a metallic glass, the structure is amorphous with no long-range atomic order. The glassy phase is formed by rapid solidification from the liquid state. The cooling rate must be high enough so that an ordered crystalline phase cannot be developed. Consequently, the thickness of a metallic glass is somewhat limited (on the order of a few millimeters to a centimeter or so) due to the need for high cooling rates necessary to freeze the molten metal into the amorphous phase. Extensive research in this area has led to the development of Bulk Metallic Glass (BMG) alloys with modest cooling rates ( $< 1$  K/sec) needed to retain the material into an amorphous state. BMG alloys have advantages in processing, similar to some advantages polymers have over traditional crystalline metals. For example, metal foams have been processed from these alloys via thermo-plastic expansion (Demetriou, *et al.*, 2007: 1). Amorphous metal foams may also be processed through routes used with other crystalline metals (Brothers, 2006; Wada, 2007). Processing advantages of amorphous alloys include higher viscosity of the melt thus minimizing sedimentation (Veazey, 2006).

A closed-cell BMG foam is considered in this investigation. In a typical foam under compression, three stages of deformation dominate: an initial elastic response, followed by a stress plateau (or slight hardening) associated with compaction, and finally stiffening due to densification (Gibson and Ashby, 1997, Miller, 2000, Gong *et al.*, 2005, Katti *et al.*, 2006). Theoretical analysis of foam mechanics has been conducted for both regular and irregular open-cell foams, with some success in determining the stress-strain relationship, especially for foams with repeated cell patterns. For example, Zhu *et al.*, (1997) considered buckling of the cell walls and modeled the nonlinear stress-strain relationship at high strains through modeling the nonlinear deformations using an approach developed by Wang and Cuitino (2000). For open cell foams, the nonlinear compressive response is governed by the buckling of cell edges (Gong and Kyriakides (2005)). Gong *et al.* (2005) modeled open cell foams using periodic, space-filling Kelvin cells based on the geometric characteristics of the actual foam. They concluded that the buckling modes are

affected by the foam anisotropy and loading conditions.

BMG foams may be formed by a thermo-plastic process that minimizes cell sedimentation and in turn offer significant control over the final microstructure (Demetriou, *et al.*, 2006). In addition, many BMG alloys exhibit stable, perfectly plastic deformation when plate thickness falls below 0.05 mm (Conner, *et al.*, 2003), as is the case for cell walls produced in these metal foams. Thus, BMG foam has some unique properties, such as low density, high specific strength, and superior thermal insulation while having control over the microstructure, so that severe cell wall deformations will potentially develop to absorb large amounts of mechanical energy before failure. Because of their amorphous structure, BMG foams also provide exceptional strength, elasticity, wear, hardness, and corrosion resistance with modest densities and low processing temperatures. They have potential for engineering applications, such as structural and biocompatible implant applications (Hanan *et al.*, 2005:2, Brothers and Dunand, 2005).

While investigations on monolithic BMG can be tracked to the 1990s, investigation of BMG foams has been initiated only recently. Work reported has been focused on improving the mechanical performance using different processing techniques and finding the relationship between microstructure and properties. For a monolithic (pore-free) BMG ( $\text{Pd}_{42.5}\text{Cu}_{30}\text{Ni}_{7.5}\text{P}_{20}$ ), Wada *et al.*, (2005) reported Young's modulus of 102 GPa, failure stress of 1.63 GPa, zero plastic strain, and rupture energy density of  $14 \text{ MJ/m}^3$ . Their results indicate that as porosity of BMG increases, both the effective Young's modulus and failure stress decrease while plastic strain at failure and rupture energy increase. Newer tougher composite BMG alloys (Hofmann *et al.* 2008) offer additional mechanical advantages, but have not been processed into foams. The ability to improve foaming to even lower densities can also lead to synergistic mechanical property improvements as thicker struts and joints are removed (Kumar *et al.*, 2010). In addition, little is known regarding the dynamic properties of these materials (Luo *et al.*, 2009). A validated numerical simulation of these foams would offer assistance in such studies.

## **2 Brief Review of Literature**

Most numerical simulations of foam materials reported in the literature were either at the macro or micro (meso) scale. At the macro scale, the foam material is considered as a continuum with homogenized properties determined from measurements, such as uniaxial compression (Gibson and Ashby, 1997). In this approach, large foam structures can be simulated at relatively low computational cost and the deformation under different loading conditions can be predicted reasonably well (Meguid *et al.*, 2002, Meguid *et al.*, 2004). As foams have different mechanical behavior under different loading conditions, for example, closed cell

polyurethane foam shows almost linear elastic behavior in tension but exhibits three stages of deformation (elastic, collapse, and densification), no unified constitutive law is available. Accurate simulations require, *a priori*, knowledge of the loading conditions. However, in some situations the associated material model may not be readily available (Wicklein *et al.*, 2004), so that simulations cannot render accurate prediction of the mechanical performance. Moreover, in such an approach, the relationship between foam microstructure and properties cannot be determined, limiting insight into the optimization of the foam microstructural design for improved mechanical characteristics.

The other approach, namely, the mesomechanical simulation approach, takes the microstructure of the foam as well as the properties of the monolith as inputs to model the macroscopic response of the foam. Microstructures can be determined based on two-dimensional images as slices of a three-dimensional foam, or based on X-ray tomography representing explicitly the mass density at each voxel of a three-dimensional image. A computational mesh is then directly generated using the three-dimensional microstructure. The discrete element/particle size is dictated by the slice thickness or the resolution of the X-ray tomography. The work using this approach is somewhat sparse, due primarily to the well-known problem associated with simulating cells in contact and large distortion involved in compaction. Among the limited publications, Kadar *et al.* (2004) investigated the mechanical behavior of closed-cell aluminum porous foam under indentation using both experimental and finite element methods and established a relationship among the shape of the deformation zone, the indenter size, and the porosity. Wicklein and Thoma (2005) used FEM to simulate the elastic and plastic response of open-cell aluminum foams and developed a relation between relative density and material properties. Use of mesomechanical approaches can provide details on the microstructural evolution during the entire deformation process. While the computational cost is high, the mesomechanical simulation is perhaps the sole choice, if explicit microstructure-property relations are sought through simulations.

For model generation using the mesomechanical simulation approach, Wicklein *et al.* (2004) described three possible approaches to discretize a foam structure into FEM meshes. In the first approach, beam and plate elements are constructed based on the cell vortices in the tomographic images. In the second approach, voxels are transformed into cubic elements in a predefined structured mesh. In the third approach, tetrahedral elements are used to mesh the entire foam structure. The second approach was used successfully for the simulation of aluminum foams (Wicklein *et al.*, 2004, Wicklein and Thoma, 2005) under a few percent deformation. However, simulation of a fully densified foam is a challenge in FEM because of large distortions of the microstructure involved and the internal contact of cell walls upon

closure of the cells. Brown *et al.* (2000) used hexahedral elements to model the struts of an open-cell foam under impact loading. The drawbacks of this approach include the use of a large number of elements and small time-steps, making it computationally intensive.

Recently, the material point method (MPM) was developed for dynamic simulations by Sulsky *et al.*, (1995) from the particle-in-cell method, and subsequently refined by others (e.g., Tan and Nairn, 2002, Wang *et al.*, 2005, Bardenhagen *et al.*, 2011). In MPM, the continuum is discretized into a finite number of material points. Each material point is represented by a Dirac delta function (zero volume). A background grid, usually a structured grid fixed in space, and a  $C^0$  continuous interpolation function are used to discretize the momentum conservation equation. When the material points move across the grid cells during deformation, numerical noise is generated due to discontinuity in the gradient of the interpolation function. Hence, in MPM simulation, stability can be adversely affected. To solve this problem, Bardenhagen and Kober (2004) introduced a  $C^1$  continuous interpolation functions in MPM, and this approach has been implemented for parallel processing using the Structured Adaptive Mesh Refinement Application Infrastructure (SAM-RAI) (Ma *et al.*, 2005).

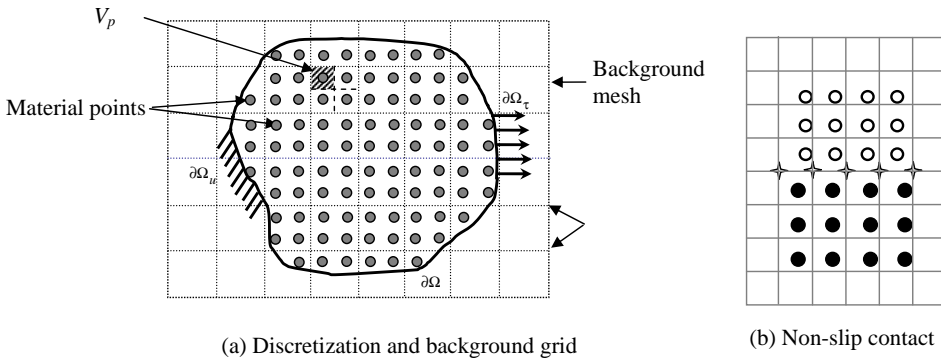


Figure 1: Illustrations of the discretization scheme and intrinsic contact in MPM.  $V_p$  is an area discretized into a material point;  $\partial\Omega_u$  is the displacement boundary, and  $\partial\Omega_\tau$  is the traction boundary.  $\partial\Omega_u \cap \partial\Omega_\tau = \emptyset$ , and  $\partial\Omega = \partial\Omega_u \cup \partial\Omega_\tau$ .

In the approach by Bardenhagen and Kober (2004), the continuum is discretized into a collection of material points with finite volume in space and a  $C^1$  continuous interpolation function is used. Figure 1 (a) is a schematic for a material continuum discretized into a collection of material points with the background grid shown. In this two-dimensional representation, an area  $V_p$  is represented by a material point.

It may be noted that material points can have different masses and different mechanical properties. Material points carry all the physical properties/variables, such as mass, displacement, velocity, acceleration, stress, and strain. Material points convect on the background mesh, usually fixed in space. Physical variables are projected on to the background nodes on which field equations, such as equations of motion are solved. The solution at the nodes is then interpolated onto the material points to allow them to move to next positions carrying updated physical variables. This process repeats until the solution is complete. When two bodies, as indicated by open and closed circles in Figure 1 (b) approach each other, the material point information on the two sides of the interface will be interpolated to the same background grid nodes in the middle as highlighted by stars in Figure 1 (b). After updating the momentum, each of these nodes has a single velocity field, for use in updating the material points on either side of the interface. As a result, the material points on either side of the interface will move subsequently following the same velocity field, leading to natural non-slip contact between the two bodies. This intrinsic feature as well as others, such as ease of discretization and no mesh distortion makes the simulation of some complex problems, such as compaction of foams possible.

MPM has been used successfully to simulate densification of open-cell foam materials (Bardenhagen *et al.*, 2005, Brydon *et al.*, 2005). In their simulations, each voxel in the X-ray tomograph is converted into a material particle and an Eulerian structured grid is used for solving the field equations. A representative volume element (RVE) was used to simulate the bulk response. Their results indicated that the apparent Poisson's ratio is negative in the stress plateau regime and the dynamic response of the compression is dominated by a compression wave, whose velocity is much lower than any characteristic wave speed, which is an inertial effect absent in a homogeneous material (Brydon *et al.*, 2005).

Numerical simulations of metallic glass foams are potentially constrained by the difficulties in modeling complex internal structures, handling large distortions as well as contact problems. However, MPM can circumvent these problems. In MPM, the model is generated by assigning a cluster of material points to regions occupied by the material so that the MPM model can be readily generated as long as the three-dimensional microstructure has been captured. The use of both Lagrangian (using material points to represent material continuum) and Eulerian (using background grid to solve field equations) descriptions makes MPM immune to mesh distortion, so that MPM gives the same results as FEM at relatively small deformations while it continues into the large deformation regime. Also, because of the use of two descriptions, points are detected as they approach and are not allowed to penetrate each other, giving MPM an intrinsic non-contact condition so that no

special contact elements are needed in the simulation of foam compaction. In this investigation, we use MPM to simulate the compression behavior of a BMG foam,  $\text{Pd}_{43}\text{Ni}_{10}\text{Cu}_{27}\text{P}_{20}$ . This closed-cell BMG foam was prepared by thermo-plastic expansion using  $\text{B}_2\text{O}_3\text{-XH}_2\text{O}$  as a blowing agent (Hanan *et al.*, 2005: 1).

The inputs for the simulation of BMG foam, using MPM, are the material properties for monolithic BMG and the microstructure of the foam. In Section 3, results of the nanoindentation experiments are presented to determine the Young's modulus of the monolithic BMG by indenting on the thick cell-walls of the foam sample. In Section 4, X-ray tomography and *in-situ* compression experiments on a BMG foam sample are presented. Section 5 describes the techniques to reconstruct the foam microstructure for simulation by creating material points from voxels in a microtomographic image. Section 6 presents the modeling techniques used and the results of compression of the metallic glass foam, at both small and large strains, using the MPM simulation method with parallel processing. First, the interpolation function of the modulus for each material point, and the minimum size of a representative volume element (RVE) are determined by comparing the stress-strain curve of the foam at the strain level of up to 3.2%. Then, material failure is introduced into the simulation to model the incipient failure observed in the experiments. Finally, the compaction of the foam is simulated using MPM up to 80% compressive strain. It may be noted that these simulations are not available in the literature either for this or for other BMG foams at large compressive strains. The simulated results are compared with the available experimental data to verify the simulation technique. Section 7 summarizes the conclusions arrived out of this investigation.

### 3 Nanoindentation on the Cell-Walls of a BMG Foam

The Young's modulus of the BMG wall, used as an input in the MPM simulation, was measured directly using nanoindentation on the cell walls of the BMG foam. This is necessary since possible interactions with the blowing agent or other peculiarities of foam processing could modify the mechanical properties compared to the monolithic solid. The foam sample was wrapped in epoxy, cured, and then cut and polished carefully to expose the cell walls. A Berkovich indenter tip was used in nanoindentation to reach an indentation depth of up to 510 nm. To enable the condition of indentation on a half-space satisfied in the analysis of nanoindentation, indentations were made only on edges of walls of at least 0.3 mm wide. Figure 2 shows the average load-depth curve with error bars from five nanoindentation measurements. Table 1 lists the data for Young's modulus and hardness for the BMG wall. The load-depth curve shows good repeatability when the depth is < 300 nm but exhibits deviation at larger indentation depths. At some locations this can be due to the presence of thinner walls so that bending could cause excessive defor-

mations to invalidate the assumption of a semi-infinite medium for nanoindentation analysis. This can lead to variation in the modulus data at larger depths. Consequently, the modulus and hardness from each nanoindentation test were averaged over depth from 100 nm to 350 nm. Within these depths, the Young's modulus did not depend on the locations in the foam wall. This modulus was used in MPM simulations. The average Young's modulus determined from nanoindentation was 108.1 GPa, close to the modulus of the same BMG monolithic solid reported elsewhere (Wada *et al.*, 2005).

Table 1: Young's modulus and hardness from nanoindentation on the cell-walls of the BMG foam ( $\text{Pd}_{43}\text{Ni}_{10}\text{Cu}_{27}\text{P}_{20}$ ). Each indentation site was selected on cell edges  $> 0.5$  mm.

| Test           | 1      | 2     | 3      | 4      | 5      | Mean            |
|----------------|--------|-------|--------|--------|--------|-----------------|
| Modulus (GPa)  | 107.36 | 98.96 | 108.23 | 108.09 | 117.86 | 108.1 $\pm$ 6.7 |
| Hardness (GPa) | 8.49   | 5.29  | 7.22   | 8.42   | 8.13   | 7.5 $\pm$ 1.3   |

#### 4 Compression Tests on the BMG Foam

The BMG foam used in this investigation had a 70% porosity, as measured by microtomographic image analysis (Hanan *et al.*, 2005:1). The cylindrical sample had a diameter of 8.08 mm and a gage length of 8.14 mm. X-ray microtomography was used to determine the internal foam microstructure, as illustrated in Figure 3. With tomography, an incident X-ray beam is partially absorbed by the sample. The transmitted X-ray beam carrying the material thickness information is transformed into visible light at the scintillator and captured by a CCD camera. A sequence of two-dimensional images were acquired as the sample rotates. Then, a three-dimensional tomographic image of the sample was reconstructed. Here, resolution was limited by the fixed field-of-view (FOV) required to illuminate up to 14 mm diameter samples. Thus, each voxel had a size of  $14.4 \times 14.4 \times 14.4 \mu\text{m}^3$  (1024 pixel image/14.7 mm FOV). Smaller (1 mm diameter) samples may be imaged down to 1  $\mu\text{m}$  resolution (Hanan *et al.*, 2005:1). However, the cell size restricted sample diameters to several mm in order to remain statistically relevant to the bulk mechanical properties. Details of the microstructure of the BMG foam will be presented in next section.

The compression velocity used in the quasi static experiments was 1 mm/s with constant displacement maintained during each irradiation for tomography. A cylindrical sample was used with the load applied in the axial direction, as shown in Figure 3. Figure 4 shows the nominal compressive stress-strain curve of the BMG

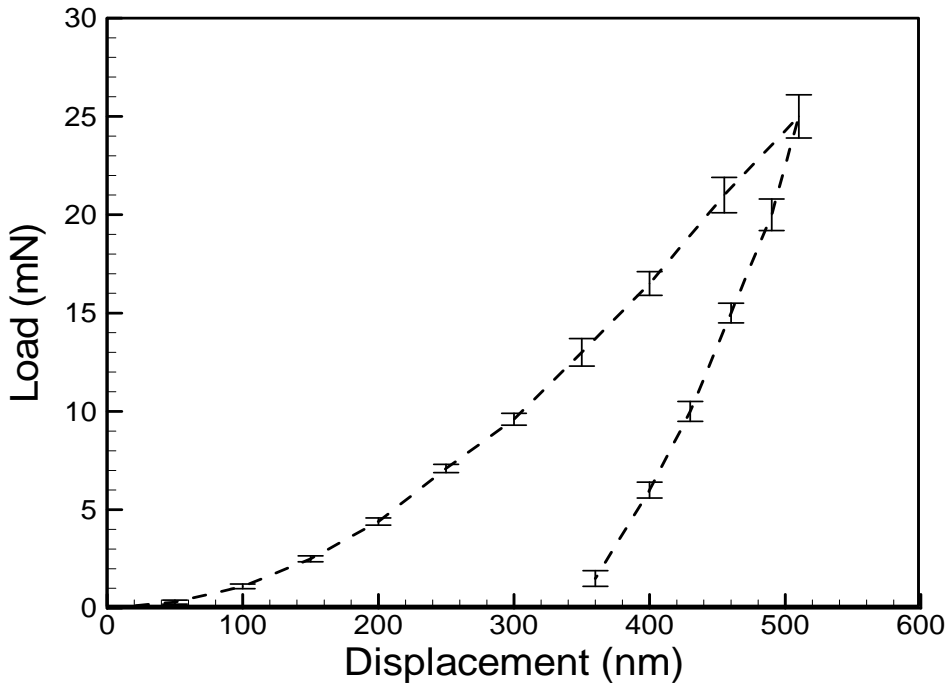


Figure 2: Average nanoindentation load-displacement curve with error bars for the BMG foam ( $\text{Pd}_{43}\text{Ni}_{10}\text{Cu}_{27}\text{P}_{20}$ ).

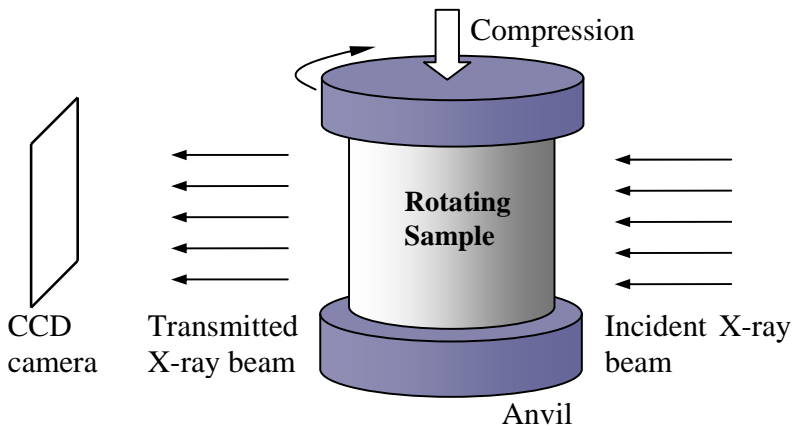


Figure 3: Schematic of X-ray tomography system with *in-situ* compression.

foam under uniaxial compression, as determined from experiment. At a compressive strain of 3.5%, there is a drop in compressive stress, marked by “slip” in the curve, corresponding to slip failure at the macroscopic level on a plane forming a nearly  $45^\circ$  angle with the axis of the cylindrical sample. The sample was unloaded before the curve could develop the typical plateau region, leaving the sample intact. The unloading curve is nearly parallel to the loading curve. A residual strain (2.3%) was observed when the sample was fully unloaded, indicating the existence of global plastic deformation in the foam. It may be noted that the foam can be re-loaded after the first slip. For ductile foams, the stress-strain curve will reach the plateau region representative of compaction process, often accompanied by multiple slips which will eventually stiffen as the internal cells close in densification.

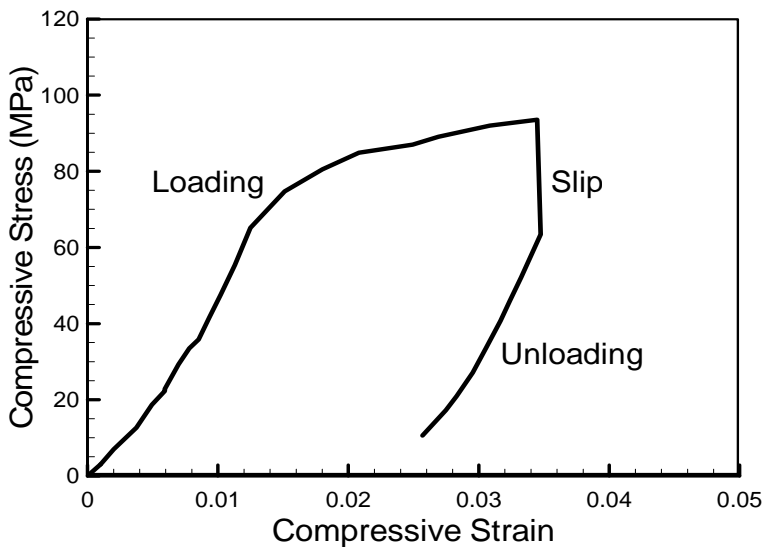


Figure 4: Experimental nominal stress-strain relationship of the BMG foam under uniaxial compression.

## 5 Reconstruction of the BMG Foam and Effect of Grid Cell Size

### 5.1 Reconstruction of the BMG foam for MPM

As mentioned earlier, the internal microstructure of the BMG foam was determined using microtomography. The voxel grayscale in the tomograph is proportional to the X-ray attenuation and represents a voxel volume averaged mass density. Figure

5 shows a portion of the microtomographic image with two neighboring sections revealed and two volume elements highlighted.

Advantage of tomography is the non-destructive ability to search through the sample to view microstructures of the foam. This allows digital measurements of the regularity of the cell shapes and characteristics of the foam. Furthermore, locations may be selected for more detailed analysis. Here, location 1 (in Figure 5) was selected to include the failure plane of the foam and location 2 was selected outside the failure plane. Later, tomographs of the sample under compression were used to identify regions including failure (Hanan *et al.*, 2005:1). While methods such as serial sectioning can be used to build initial microstructural models, only non-destructive methods can be used for conclusively identifying the regions of failure.

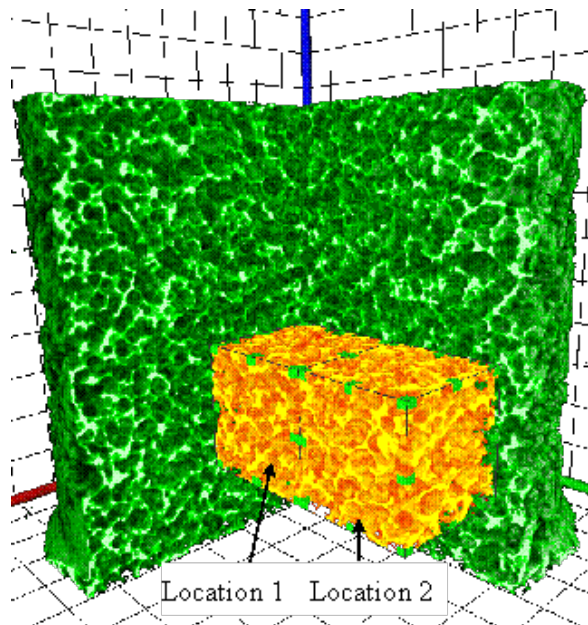
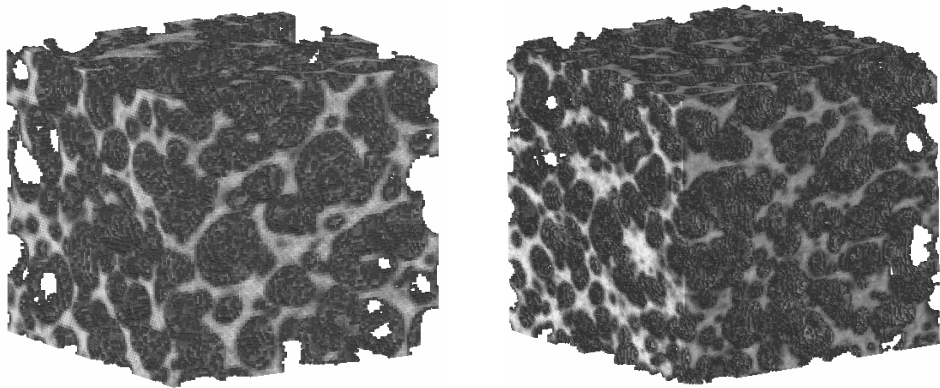


Figure 5: Three-dimensional microtomographic image of a BMG foam at zero strain with two volume elements highlighted. The background grid spacing is 0.9 mm.

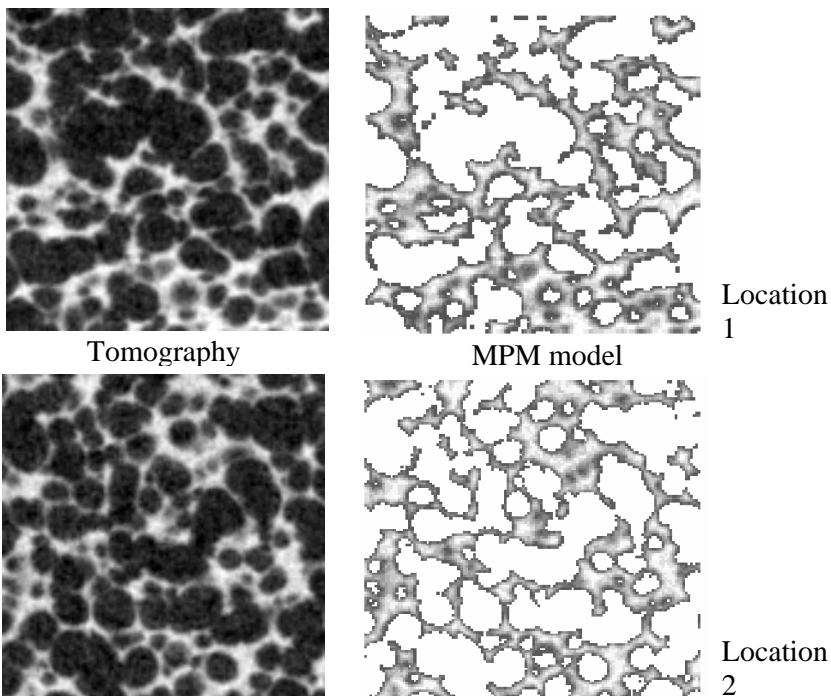
Figure 6 (a) shows two reconstructed MPM images at two points and Figure 6 (b) shows the comparison of a section at each point. The raw tomographs are recon-



Location 1

Location 2

(a) Reconstructed three-dimensional MPM models



Tomography

MPM model

Location 1

Location 2

(b) Comparisons of sections between tomographic images and reconstructed models

Figure 6: Tomographic images and three-dimensional reconstructed MPM images at two locations for comparison.

structed from 12 bit images. This dynamic range allows a clear division between the voids and the solid material. The cut-off value that produces a porosity of 70% in the MPM models was 20% of the full scale intensity (2.78 in floating point), where solid walls characteristically gave values above 7. The voxels with a grayscale value less than 2.78 were not converted into material points in Figure 6 (b). It may be noted that a tremendous amount of computational time is needed to simulate the entire volume observed with tomography due to limitations on the number of processors available. To circumvent this, a small volume element of  $100 \times 100 \times 100$  voxels (representing a  $1.44 \times 1.44 \times 1.44 \text{ mm}^3$  cube at least 6 average cell diameters across) was used first in the simulation. The effects of size and location of the volume element were investigated subsequently. Solid Pd-based BMG has a density of 9.44 g/cc. Material points were assigned to areas occupied by the BMG foam matrix. For the simulations, 12 processors (Pentium IV, 2.4 GHz, 512 MB memory) were used in parallel and the computational domain was divided into approximately equal-sized blocks, e.g. 3, 2, and 2 in the  $X$ -,  $Y$ -, and  $Z$ - directions, respectively. Details on parallel processing in MPM can be found in Ma *et al.* (2005).

## 5.2 Effect of grid cell size on simulation convergence

In MPM simulations, accuracy increases with finer background grid, since the momentum conservation equation is solved at each grid node. In the MPM computation, interpolation of physical variables is made between material points and their neighboring nodes. The computational time depends directly upon the number of background grid nodes and the grid size. When the grid size is small, physical variables of material points, such as the stresses and strains are interpolated on a large number of grid nodes resulting in more computations. Numerical simulations were first conducted to determine the effect of grid size on accuracy. A normal traction of 50 MPa was applied at one end of the sample in the  $Z$ -direction to pull the sample. The time step and the numerical damping factor used were 0.5 ns and  $1000 \text{ s}^{-1}$ , respectively.

The normal stress  $\sigma_z$  on a given cross-section, after 1000 increments, is plotted in Figure 7 using grid sizes of 3 and 4 times the voxel size ( $14.4 \mu\text{m}$ ) in each direction. The material points are plotted according to their spatial location and different colors represent the magnitude of  $\sigma_z$  stress. In Figure 7 (a) and (b), stress oscillations, as indicated by the dashed circles, can be seen. These oscillations, on the order of the grid size, are aphysical due to local interactions of the material points near the cells. It may be noted that the surface of a cell is traction-free but if the grid is too coarse, the material points on both sides of a cell can interact with each other through the grid node. This results in early contact and non-zero traction on the surface of a cell and violates the traction-free conditions on the surface.

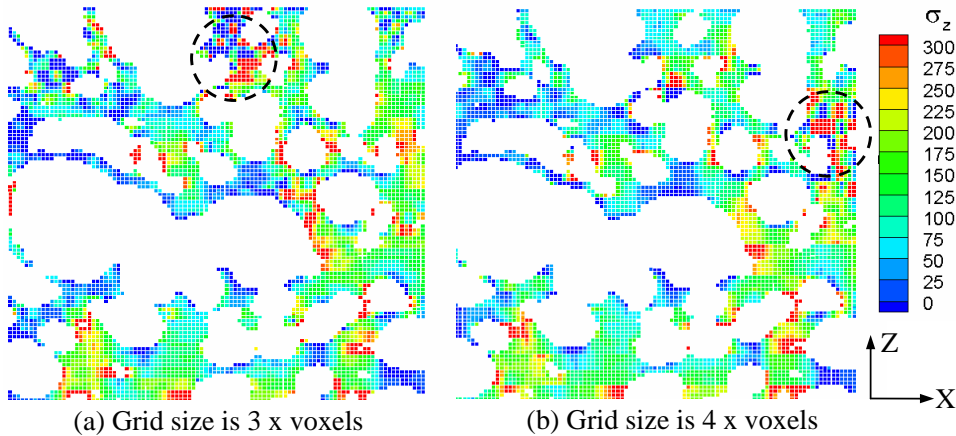


Figure 7: Stress distribution on a section of the three-dimensional model simulated with the grid size 3 times (a) and 4 times (b) the voxel size.

These results indicate that the grid size is too large. To circumvent this problem, smaller grid sizes were investigated. Figures 8 (a) and (b) show the normal stress distribution on the same section as used in Figure 7 (a) and (b), but simulated with the grid size of 1 and 2 times the voxels in each coordinate direction, respectively. The results show that transition is smooth. Comparison of Figures (a) and (b) shows that  $\sigma_z$  stress is almost zero on the cell top/bottom surfaces when the grid size is 1 voxel, which means the traction-free boundary condition on the surface of each cell is satisfied.

The average computational times per time step were 8.8, 9.2, 10.5, and 13 s for grid sizes of 4, 3, 2, and 1 voxel, respectively, while all other conditions remaining the same. It can be seen that the computational time increases with decrease in grid size. Brydon *et al.* (2005) showed that if the grid size is two thirds of the voxel size, then there is no appreciable improvement in the accuracy. In their work, an average cell crossed 19 grid elements and captured the material response. Here, most of the smaller cells cross 10 grid elements at the 1 voxel grid spacing with an average cell containing 16 grid elements. For a balance between accuracy and computational time, the grid size was set to one voxel size in subsequent simulations.

Next, a simulation of compression was performed with displacement boundary conditions applied on the top to compress the volume element, using the penalty method (Ma *et al.*, 2006). In this simulation, 12 uniform layers of material points of the same properties were added above the volume element and the displacement boundary conditions were applied on the top surface. Figure 9 shows the stress dis-

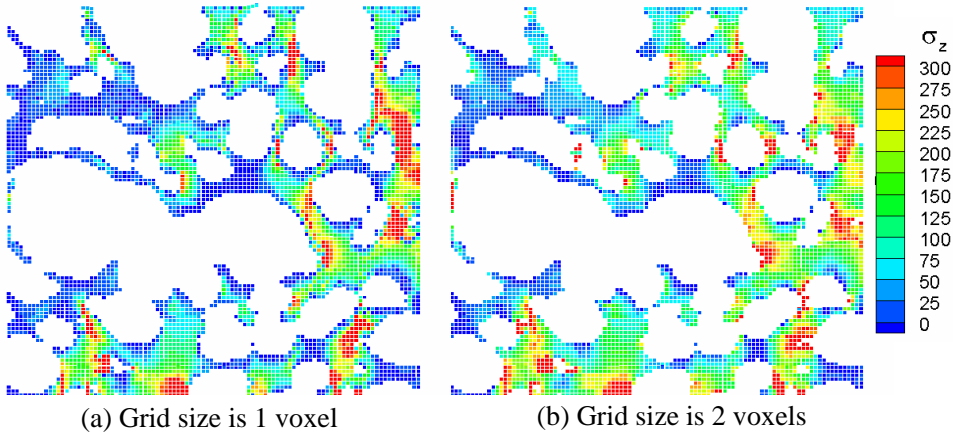


Figure 8: Stress distribution on a section of the three-dimensional model simulated with the grid size 1 and 2 times the voxel size ( $14.4 \mu\text{m}$ ).

tribution in the overall three-dimensional MPM model at  $t = 2.5 \mu\text{s}$  with a nominal compressive strain of 0.625%.

Distributions of the stresses and deformations in the BMG foam were determined for each cross section. For discussion, each section is identified for simplicity by its normal direction and a number. The number between 0 and 100 indicates the percent location of the section along the specified direction. For example, section  $X - 20$  represents the cross section perpendicular to the  $X$ -axis and located at 20% of the depth of the cube sample in the  $X$ -direction. Figure 10 shows the  $\sigma_z$  stress distribution of two sections at  $t = 2.5 \mu\text{s}$ , when the average compressive strain is 0.625%.  $\sigma_z$  stress tends to align with the available vertical paths. About 50% of the foam is under stress while the rest does not play much role in carrying the stress at this time. Along the path, where the stress is higher, the foam wall is generally thinner. It can be seen from Figure 10, the traction-free boundary condition on the cell surfaces remains well satisfied in the compression simulation with the grid size set at one voxel size.

## 6 Simulation of the BMG Foam in Compression

This section describes the simulation of the BMG foam in compression. The time step,  $dt$  used in the simulation was 0.5 ns, which was determined from the longitudinal wave speed,  $C_l$  and the grid size,  $L_g$ , through  $dt = k \cdot L_g / C_l$ , where  $k \leq 1$  is a constant factor and the longitudinal wave speed of bulk BMG is 3926 m/s. If the actual velocity used in the experiments was taken in the simulations, the com-

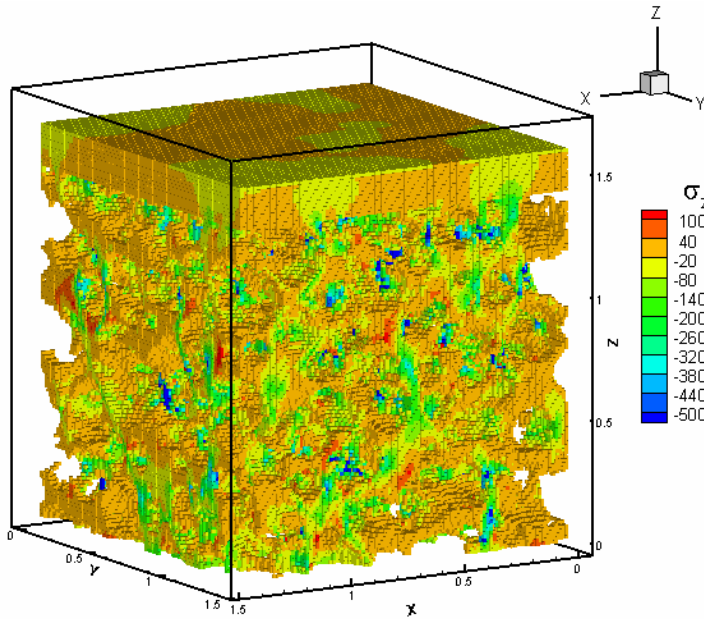


Figure 9: Stress distribution (in MPa) in the foam in the overall MPM model at 0.625% compressive strain.

putational times would be very long to reach a compressive strain of 10% because a very large number of time increments would be required due to the use of small time steps. To reduce the computational time, the maximum velocity applied was set at 20 m/s, which is 0.5% of the longitudinal wave speed of the solid BMG. To reduce the initial impact, the applied velocity was increased linearly from 0 to 20 m/s in 10  $\mu$ s. From the simulation, the total force  $\mathbf{F}$  was computed as

$$\mathbf{F} = \sum_i \mathbf{A}_i \sigma_i \mathbf{n} \quad (1)$$

where  $\mathbf{A}_i$  is the area of the top surface of material point  $i$ ,  $\mathbf{n} = (0, 0, 1)$  is the unit outward normal vector, and the summation is performed over all the material points on the actual top cellular layer of the volume element. The average stress is the total force  $\mathbf{F}$  divided by the gross cross sectional area. The average compressive strain was computed as the average relative displacement of both cellular end surfaces divided by the initial height of the cellular volume element.

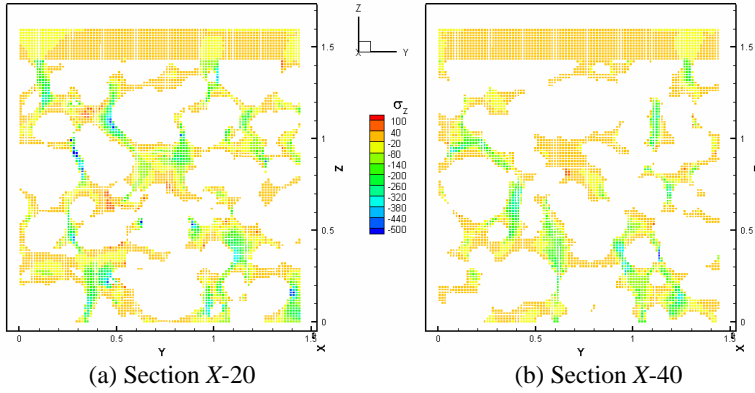


Figure 10: Stress distribution in typical sections at 0.625% compressive strain ( $t = 2.5 \mu\text{s}$ ).

### 6.1 Elastic and plastic properties

Each voxel occupied by the material is assigned a material point. The mass density and Young's modulus of each material point depends on the grayscale of the voxel. Since the BMG alloy represents a single attenuation length, the mass density of the material point is linearly dependent on the grayscale. The Young's modulus of each material point is assumed to obey a power law relation with the grayscale, i.e.,

$$E_p = \left( \frac{s}{I_{\max}} \right)^n E \quad (2)$$

where  $s$  is the grayscale of a voxel and  $I_{\max}$  is the maximum grayscale corresponding to the density of the bulk solid material. When the exponent  $n = 1$ , the modulus is linearly dependent on the grayscale. This is consistent with the rule of mixtures (Jones, 1999) where each voxel is occupied by the material and air. For a closed-cell foam, the modulus for a volume element containing a cell can be taken to be proportional to the square of the volume fraction (Gibson and Ashby, 1997, Wicklein and Thoma, 2005). Hence, in this study, the exponent  $n = 2$  is also simulated and reported in the next section for comparison. Cells below 0.03 mm have been observed in this system (Hanan *et al.*, 2005:1). The mean Young's modulus  $E$  used for the BMG foam is 108.1 GPa (see Table 1) and the Poisson's ratio of the monolithic BMG is assumed to be 0.3.

The bulk metallic glass (BMG) alloy is linearly elastic and brittle, with the plastic strain at failure nearly equals to zero in compression (Wada *et al.*, 2005). However, Wada *et al.*, (2005) reported that the ductility of BMG ( $\text{Pd}_{42.5}\text{Cu}_{30}\text{Ni}_{7.5}\text{P}_{20}$ ) can be

improved by introducing micro pores because the pores force the proliferation of shear bands below the failure stress, which toughens the alloy. Their experimental results showed that plastic strain at failure increases to more than 18% with increase in porosity from 0% to 3.7%. The ductility of the BMG foams under uniaxial compression is significantly higher than under tension. Wada and Inoue (2003) reported 90% nominal compressive strain without macroscopic failure and Brothers and Dunand (2005) reported 50% nominal compressive strain for several BMG foams.

The ductility and failure strain of BMG have been reported to depend on the wall thickness (Conner *et al.*, 2003). In the simulation, the yield strength of the monolithic Pd<sub>43</sub>Ni<sub>10</sub>Cu<sub>27</sub>P<sub>20</sub> BMG is assumed to be 1.63 GPa, based on the experimental results on a pore-free Pd<sub>42.5</sub>Cu<sub>30</sub>Ni<sub>7.5</sub>P<sub>20</sub> BMG (Wada *et al.*, 2005). von Mises plasticity with isotropic bilinear hardening is used and the hardening modulus is assumed to be 5% of the Young's modulus based on the measurements on similar materials (Wada *et al.*, 2005).

## 7 Determination of the interpolation exponent and the minimum size of a representative volume element (RVE)

In this section, numerical simulations are presented to determine the appropriate choice of the value of the interpolation exponent  $n$  in Eqn. (2). The minimum size of a representative volume element (RVE) is also determined based on the convergence of the simulation results. A minimum in RVE ensures both efficiency and accuracy and it is used in future simulations.

Two locations in the foam, as shown in Figure 5, were chosen in the simulations. The first location encompasses a slip plane as observed in *in-situ* tomography of the foam in compression and the second location is close to the first location but farther away from the slip plane. Several simulations were conducted using volume elements of different size (cubes of 40, 60, 80, 100 and 120 voxels in each coordinate direction) at these two locations in an effort to determine the minimum size of a representative volume element (RVE). The computed porosity for each volume at both locations is given in Table 2. Porosity for different sizes at each location deviates from the nominal value due to randomness in the internal complex structure of the BMG foam, but as the volume increases to 120<sup>3</sup> voxels (1.73<sup>3</sup> mm<sup>3</sup>, the distance between voxels is 0.014 mm), the porosity at these two locations converge to values very close to 70%, the nominal porosity of the foam. Both cell size and shape vary significantly. Measured from the three-dimensional plots, minimum diameter of the cells was three voxels (0.043 mm) at these two locations, and the maximum dimension of the cells was ~ 80 voxels (1.15 mm). The aspect ratio, defined by the maximum dimension divided by the minimum dimension, is as

large as 6 to 10. The average cell dimension was 0.23 mm, equivalent to 16 voxel lengths. For location 1, the minimum length of the cubic volume, representative of the bulk porosity of the BMG foam, is 7 to 8 times an average cell size.

Table 2: Porosity of different size volume elements at two locations.

| Side length (voxels)      | 40    | 60    | 80    | 100   | 120   |
|---------------------------|-------|-------|-------|-------|-------|
| Volume (mm <sup>3</sup> ) | 0.19  | 0.65  | 1.54  | 3.01  | 5.20  |
| Location 1                | 78.7% | 73.0% | 73.2% | 73.4% | 71.4% |
| Location 2                | 72.8% | 69.8% | 69.3% | 70.2% | 70.4% |

Figure 11 shows the stress-strain curves from simulations using a second order interpolation of the modulus, i.e.,  $n = 2$  in Eqn. (2). Slopes from the simulations are all smaller than the initial slope of the loading portion of the experimental curve. The simulation curves from volume elements of sizes 60, 80, and 100 approach the same modulus at location 2. However, the slope obtained from a volume element of 40 voxels is much smaller at this location. It can be seen from Table 2, the sample porosity at location 2 does not vary much when the sample size is between 60 and 120 voxels. The macroscopic yield strength determined from a volume element of 100 voxels is close to the stress at the onset of macroscopic collapse from experiment. At location 1, where the slip plane was observed, the slopes increase with the size of the volume element. The 120-voxel element, at location 1 that includes the slip plane, gives the converged stress-strain curve, comparable to the 100-, 80-, 60-voxel elements at location 2 that does not include the slip plane.

Thus, selection of an RVE is dependent upon the presence of weakness in the local microstructure, which may lead to failure as observed in location 1 and evident by the local increase in relative density. Smaller RVE's aid in numerical simulations since the computation time is proportional to the number of material points. A small RVE size of side length 60 voxels corresponding to less than 4 average cell diameters is sufficient for describing the elastic behavior of the foam for locations outside the failure plane. However, for locations including the failure plane, the RVE necessary for adequate simulation of yielding in the foam is found to be 120 voxels across, corresponding to 7.5 average cell diameters. This result confirms the experimental observation found in other metallic foams indicating edge effects which tend to dominate when a specimen dimension falls below 7 cell diameters (Ashby, *et. al*, 2000).

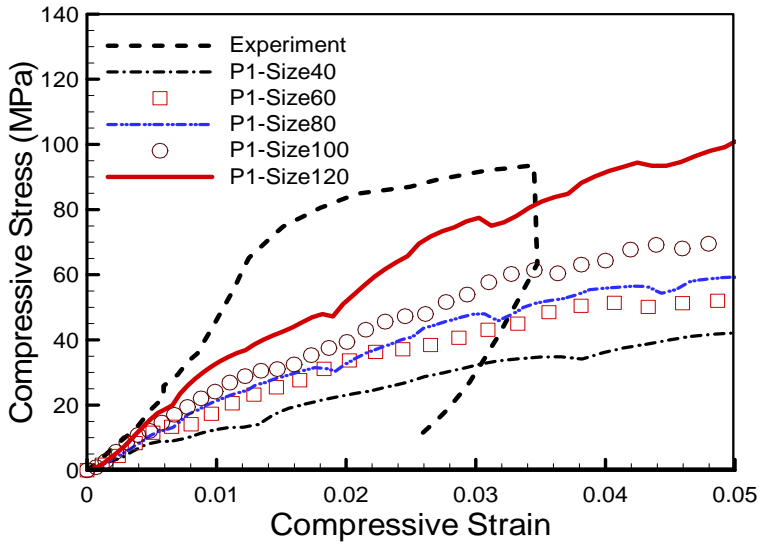
As shown in Table 2, location 1 includes a sub-region of greater relative porosity, up to 79%. In this case, tomography was performed during and after failure, so that the specific location of the failure plane is known. Observation of local density

variations can be a useful indicator of likely failure sites in future investigations. Without including local weaknesses in the microstructure, the global behavior of the foam can not be simulated correctly (see Figure 11). To correctly simulate the global behavior, not only must the local density match the global value, but the RVE must include a representative version of the microstructure likely to fail.

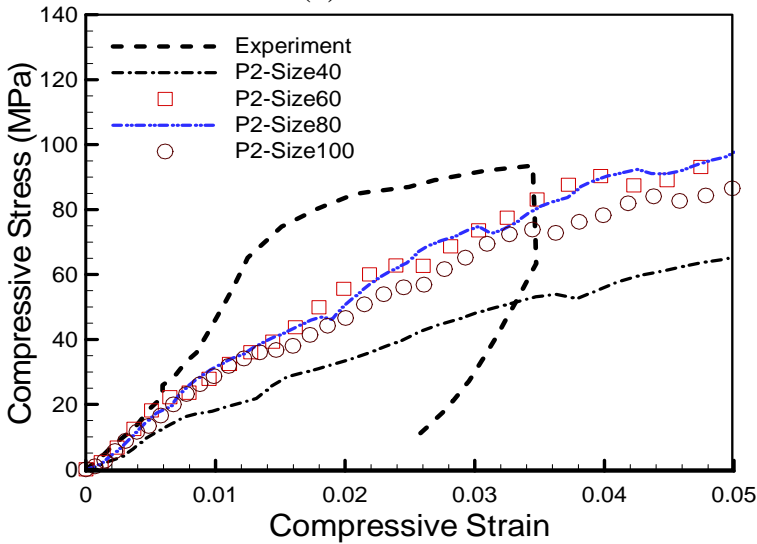
Figure 12 shows the simulation results using linear interpolation for the modulus of each material point. It can be seen that the stress is higher at the same strain when the volume element is larger at location 1. For the size of 120 voxels, the compressive stress-strain curve is very close to those of location 2. In general, the simulated curves for sizes 100 and 120 voxels at location 2 compare well with the experimental curve.

From these comparisons, it is concluded that linear interpolation of the modulus is appropriate for the simulation. In monochromatic tomography of single phase materials, the grayscale of a voxel is linearly related to the volume and mass of the material in this voxel. Using linear interpolation for the modulus is equivalent to applying the rule of mixture to compute the modulus ( $E = f_1 E_1 + f_2 E_2$ ) with  $f_1$  the volume fraction of amorphous metal with modulus  $E_1$ , and  $f_2$  the fraction of the voids with zero modulus ( $E_2 = 0$ ). Second order interpolation of the modulus for each material point (voxel) gives a smaller modulus than the linear interpolation. The stress-strain curves using the second order interpolation are softer than the ones using linear interpolation. Second order interpolation is more suitable when the voxel contains a complete cell (Gibson and Ashby, 1997, Wicklein and Thoma, 2005). Here, all cells are larger than the voxel dimensions. Hence, it is the first order interpolation that is appropriate for the modulus. The stress-strain curves from a volume element of side length 120 voxels (7.5 cell diameters) converge at both locations, no matter which interpolation of the modulus is used. The  $120^3$ -voxel element can be used as a representative volume element. However, the stress-strain curves from the simulations also depend on the location and porosity of an RVE. For the location without a macroscopic slip plane, the RVE size can be smaller. Both Figure 13 and Figure 14 show that the convergence for the RVE with the slip plane (location 1) is slower than the RVE without the slip plane (location 2), which has been reported by Gong, Kyriakides and Triantafyllidis (2005). The RVE porosity can be used as an additional condition for determining the minimum RVE size.

Figure 11 and Figure 12 show the  $\sigma_z$  stress distributions at different compressive strains on a section at locations 1 and 2, respectively. It is seen that under compression, the stresses increase monotonically with strains. The stress path and the section shape do not change during elastic compression.

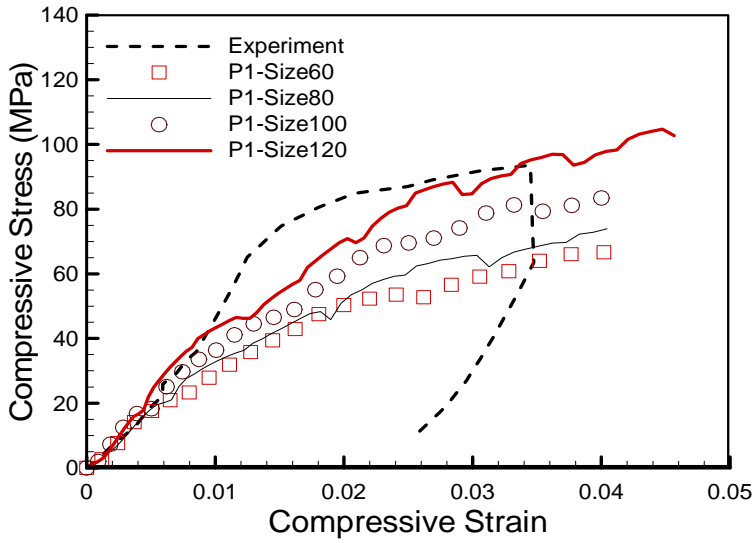


(a) Location 1

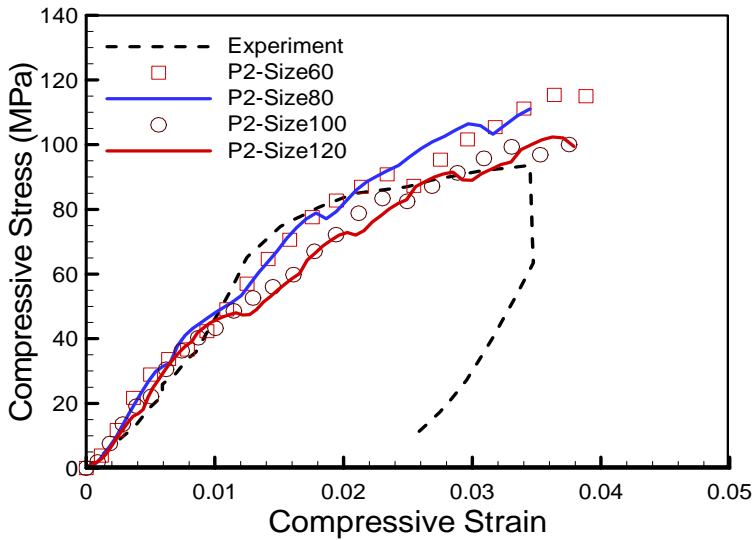


(b) Location 2

Figure 11: Stress-strain curves of the BMG foam from experiments and simulations using second order interpolation.



(a) Location 1



(b) Location 2

Figure 12: Stress-strain curves of the BMG foam from experiments and simulations using linear interpolation at two locations.

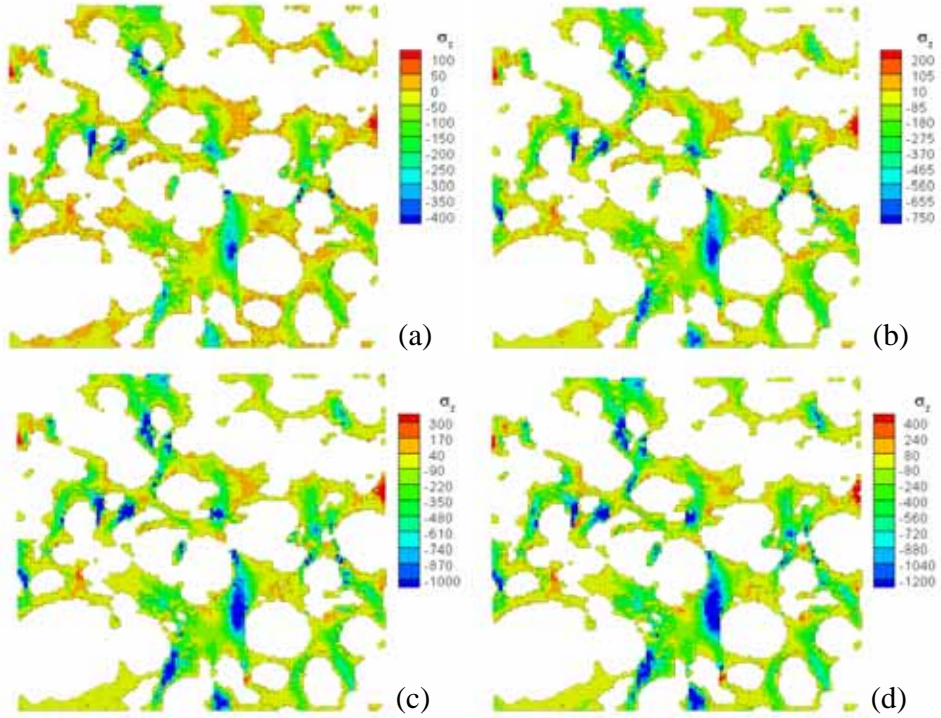


Figure 13: Stress distribution on a section at location 1 (a) compressive strain = 0.5%, (b) compressive strain = 1.2%, (c) compressive strain = 2.1%, (d) compressive strain = 3.3%.

### 7.1 Deformation Mechanisms and Material failure of BMG Foams

Incipient shear failure was observed under uniaxial compression of BMG foams (Demetriou *et al.*, 2007:2). However, accurate failure modes of BMG foams are still under development. In this study, a shear failure mode associated with the von Mises plasticity (ABAQUS, 2005) is used. A strain based damage parameter  $\bar{\omega}$  is defined as

$$\bar{\omega} = \frac{\sum \Delta \bar{\epsilon}^{pl}}{\bar{\epsilon}_f^{pl}} \quad (3)$$

where  $\bar{\epsilon}_f^{pl}$  is the strain at failure for the material and  $\Delta \bar{\epsilon}^{pl}$  is the equivalent plastic strain increment. When the damage parameter  $\bar{\omega}$  at a material point exceeds one, this point is considered to have failed and is eliminated in subsequent computations.

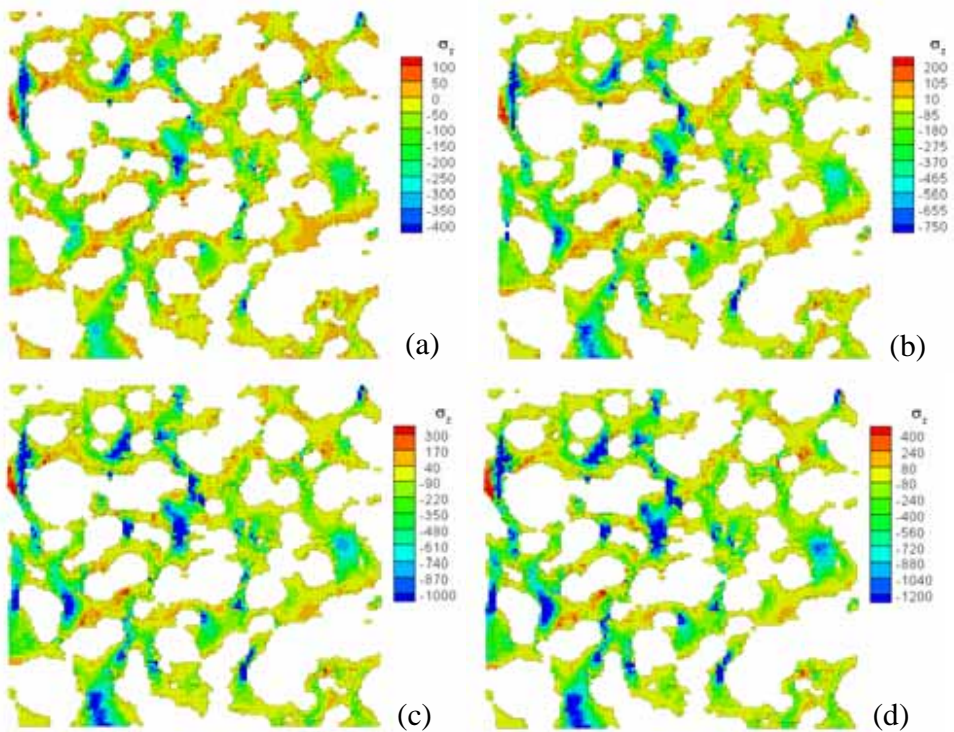
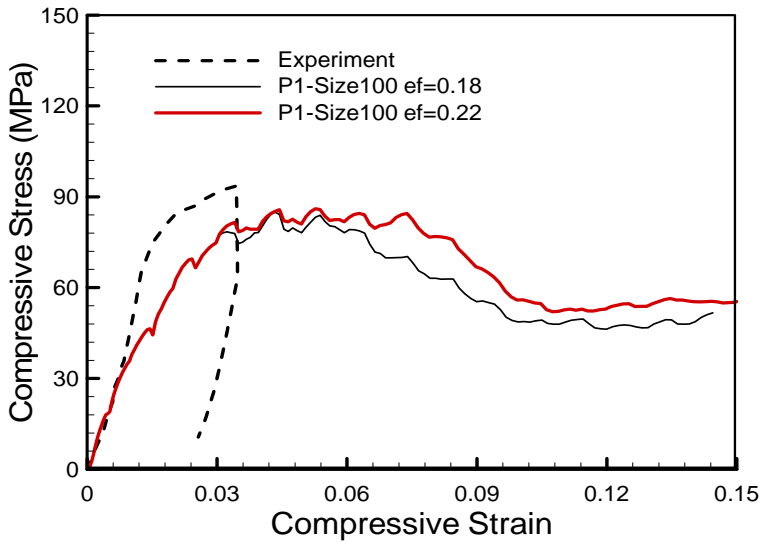


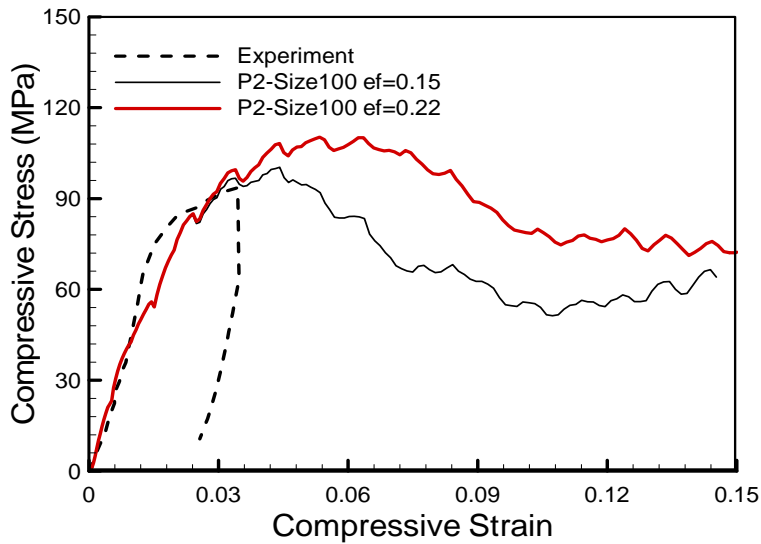
Figure 14: Stress distribution on a section at location 2, (a) strain=0.5%, (b) strain=1.2%, (c) strain=2.1%, (d) strain=3.3%.

The ductility of metallic glass is a function of the dimensions, such as the wall and plate thicknesses or diameter of a BMG wire. The value of  $\bar{\epsilon}_f^{pl}$  is a function of the thickness based on uniaxial ductility data of similar materials (Conner *et al.*, 2003) and a value in the range of 0.12 and 0.22 was chosen for the simulations.

Figure 15 shows the compressive stress-strain curves for two volume elements with the strain at failure,  $\bar{\epsilon}_f^{pl}$  between 0.15 and 0.22. A 30 MPa drop of the stress is seen in each of the simulations and the starting strain of the stress-drop is smaller, if  $\bar{\epsilon}_f^{pl}$  is smaller. The amount of drop in stress is close to the experimental value. The initial portion of the stress-strain curve is not affected by failure strain. With continued applied load after the drop, the stress reaches a plateau region. In the experiments, the applied load was released after the first collapse was observed. As the height of the volume element is only a fraction of the entire sample, the nominal strain increment corresponding to the stress drop associated with collapse is larger than the experimental value, resulting in a different slope in the stress-strain curve.



(a) Location 1



(b) Location 2

Figure 15: Simulation results showing the compressive stress as a function of compressive strain using shear failure criterion.

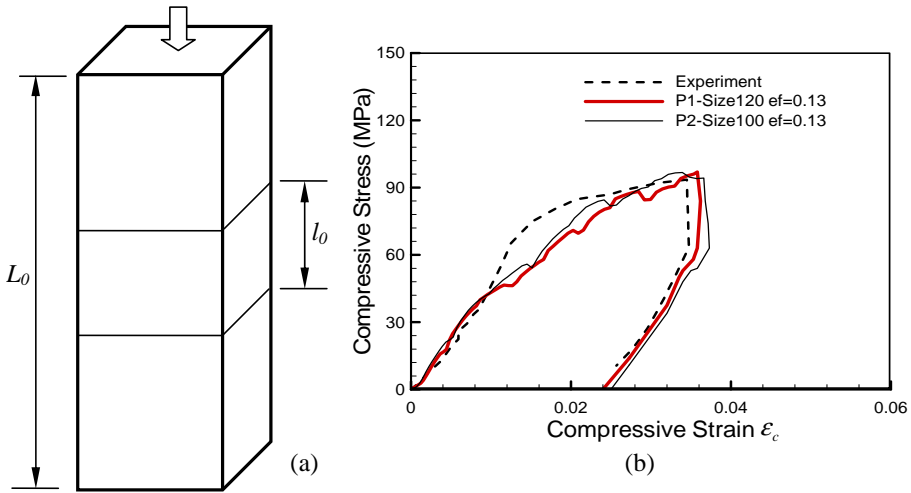


Figure 16: (a) A stack of RVE’s to the gage length of the entire sample and (b) the total stress-strain curves.

Since the failure in the foam is incipient and localized, it is possible to correctly simulate the slope of the compressive stress-strain curve during the stress drop reusing only the results of the RVE. Figure 16 (a) shows a stack of  $n$  RVE’s in the axial direction to the gage length of the sample. Failure occurs in one RVE and the other RVE’s still undergo uniform deformation. The total displacement during the slip can be computed from

$$\Delta L = \Delta \epsilon_1 l_0 + (n - 1) \Delta \epsilon_0 l_0 \tag{4}$$

where  $\Delta \epsilon_1$  is the compressive strain increment for the RVE with failure and  $\Delta \epsilon_0$  is the compressive strain increment for the other RVE’s without failure. Note that  $\Delta \epsilon_0$  is negative due to the stress drop and its value can be obtained from the stress-strain curve. The overall nominal compressive strain can be computed as  $\Delta \epsilon = \Delta L / L_0$ . Figure 16 (b) shows the total stress-strain curves including unloading, confirming good agreement between simulation and experiment. It can be seen that the data at location 1, which includes the macroscopic failure plane, is closer to the experimental curve.

Deleting material points due to failure, violates conservation of mass in the simulations. However, it is an effective approach when the loss is negligible for small strains. Since in experiments, material is still present after failure, some of the failed materials, i.e., failed cell walls, may carry load again under large compressive strain upon contact with other cell walls. If deletion of material points is used

at large strains (>20%), potentially achievable with amorphous metal foams, simulation errors may become significant due to this cumulative loss in mass.

## 8 Simulation of compaction

Structural foams can absorb energy when subjected to compressive loading. Numerical simulations of the compression process can facilitate in the determination of the energy absorbed by a foam. Simulation of compactions involves large deformations and internal contacts due to closure of the cells. MPM can overcome these two challenges because of its inherent capabilities of handling the internal contact using the natural non-slip contact. The material failure model deletes all the failed material points and this can lead to significant loss of mass during compaction simulation. Hence, material failure is turned off in this simulation by setting the failure strain to infinity. Due to lack of effective modeling of successive incipient slip failure in the foam, the compaction simulation in this study may not represent the actual behavior of the bulk metallic glass foam under compressive strain. But in the development of the BMG foam it is the goal to reach high value in compressive strain for applications, such as energy absorption on impact. This simulation can shed light on the prediction of the mechanical behavior of a ductile BMG foam.

To minimize the computation time, the RVEs at both locations were used in the simulations executed on 16 processors. The stress-strain curve from the compaction simulation is shown in Figure 17, where the three stages, i.e., elastic, plateau, and stiffening can be seen clearly. Similar stress-strain relations were reported for other BMG foams (Brothers and Dunand, 2005, Brothers and Dunand, 2006). The stress-strain curves from simulations at two locations agree, in general, with each other. Figure 18 shows the deformation at location 1 for increasing nominal compression strains. The deformations of section Y-50 for location 2 are illustrated in Figure 19. In the compaction process, the foam walls were bent and distorted significantly leading to closure of the internal cells. Consequently, the walls come in contact with each other and the stiffness of the foam increases, resulting in stiffening in the stress-strain curve. In Figure 17, the stiffening process commences at 35% compressive strain and completes close to 70% compressive strain when the slope of the stress-strain curve cease increasing. Since the porosity is approximately 70%, most of the internal cells are closed at 70% compressive strain. By integrating the stress-strain curves in Figure 17 up to 80% compressive strain, the absorbed energies per unit volume at locations 1 and 2 are  $165 \text{ MJ/m}^3$  and  $167 \text{ MJ/m}^3$ , respectively. The good agreement in absorbed energy per unit volume at two locations indicates that RVE's chosen at small strains can be used for simulation at large strains.

Figure 19 shows the progression of the deformation for section Y-50. The colors represent the magnitude of the maximum shear stress  $\tau_{\max}$  at any given location.

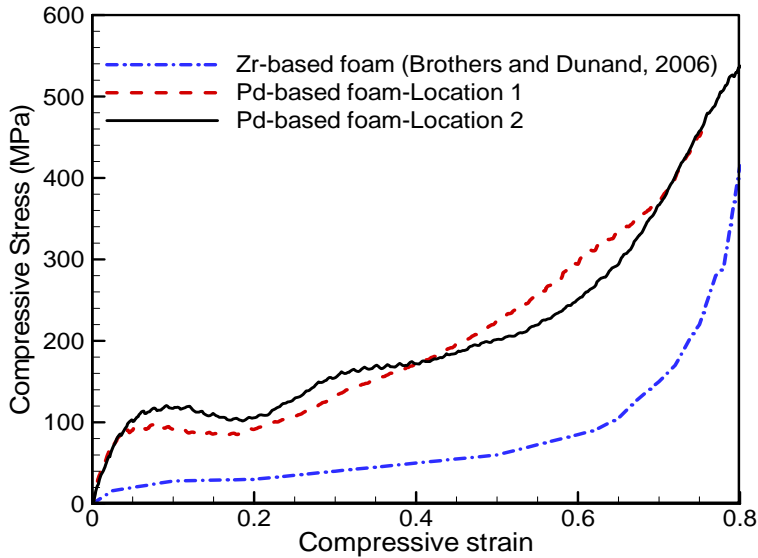


Figure 17: Stress-strain curve from the compaction simulation.

At 4% nominal compressive strain ( $\epsilon_c$ ), most of the material points on this section are not carrying much stress and the path of the greatest stress can be clearly seen. The wall of one cell, which is indicated by the arrow, is the only ligament on this section connecting the top and bottom parts. At 12% compressive strain, a localized band of high stress (red color) is developed on this cell edge. At 21% compressive strain, it has bent and the walls to the left have made contact. The shear stress continues to develop in this area at 31% compressive strain. The closure process of the marked cell can also be seen in these plots from 12% to 49% compressive strain. The analysis of the maximum shear stress can be used to predict the incipient shear failure or shear banding of the matrix, as observed in experiments (Brothers and Dunand, 2005, Demetriou *et al.*, 2007:2). The high stress areas (indicated by the red spots) are the candidates for future failure analysis studies. As observed in the tomography, the walls can buckle in compression. The last four plots in Figure 19 shows buckling of one wall on the side of the volume element, as indicated by the solid circles.

The  $\sigma_z$  stress distribution on section Y-50 at location 2 is shown in Figure 20. The nominal stress-strain curve from 12% to 31% compressive strain is in the plateau region, i.e., the stress is almost constant. It can be seen from Figure 20 that both negative and positive  $\sigma_z$  stresses increase in magnitude. This levels out the overall stress. From 49% to 66% strain, more and more cells are being closed. The nega-

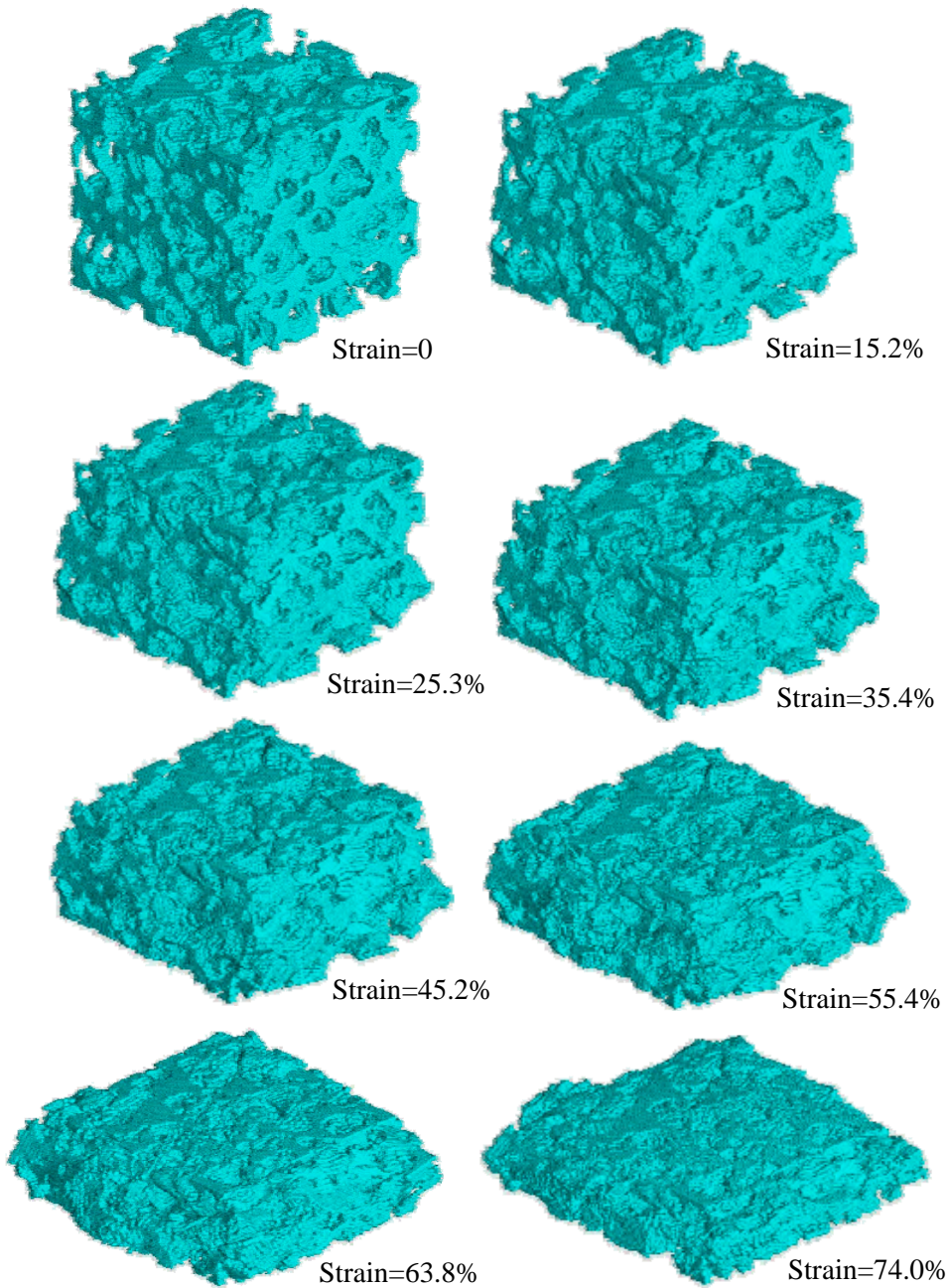


Figure 18: Deformed three-dimensional MPM models for increasing compressive strains at locations 1 and 2 which appear similar.

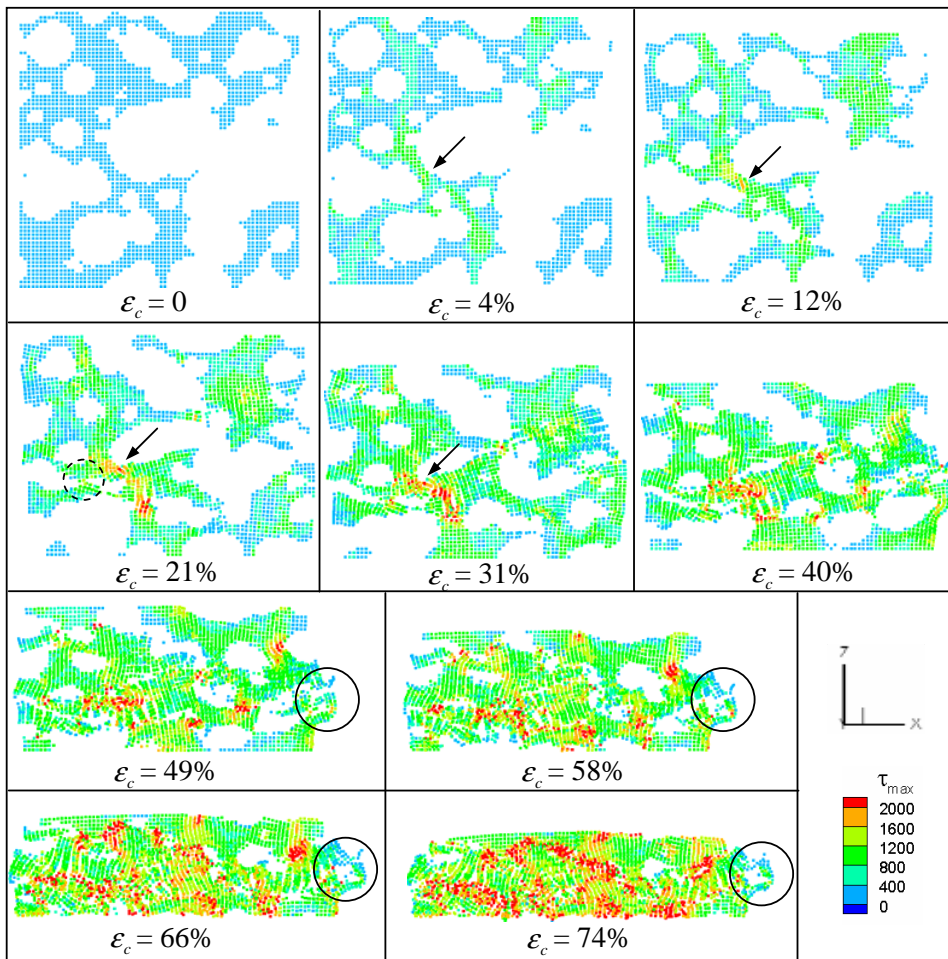


Figure 19: Maximum shear stress on section Y-50 at location 2 at different compressive strains.

tive  $\sigma_z$  stress continues to increase in magnitude but the number of material points carrying positive  $\sigma_z$  stress decreases. The overall response of the volume element becomes stiffer. At 74% compressive strain, which is near full compaction, most of the material points are carrying compressive  $\sigma_z$  stress with higher magnitudes. At this strain, the stiffness of the volume element approaches the maximum, as measured from the slope of the stress-strain curve in Figure 17.

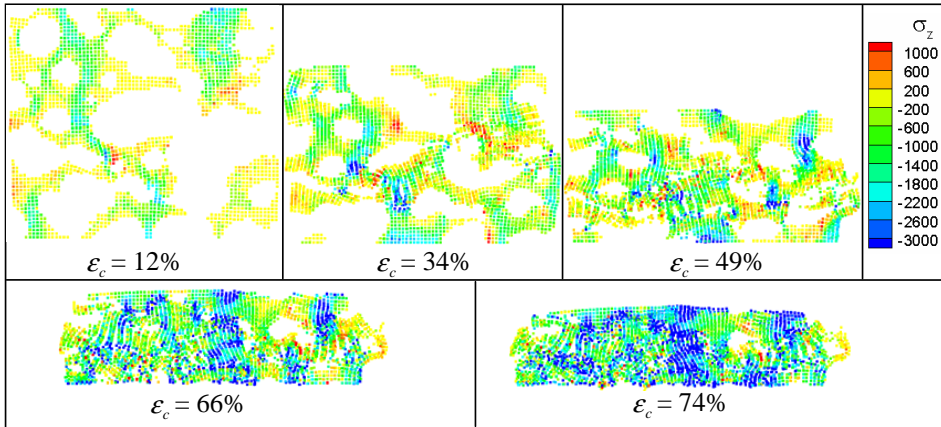


Figure 20: Distribution of  $\sigma_z$  stress on section Y-50 at location 2 at different compressive strains.

In order to observe more clearly, the distribution of compressive and tensile stresses throughout the volume, a histogram of the strains was plotted. Figure 21 shows the percentile distribution of the strain component  $\epsilon_z$  at different nominal strains at location 2. The vertical axis indicates the percentage of material particles with a strain of  $\epsilon_z$ . As the nominal compressive strain increases, more and more material points, in general, are under compression (negative  $\epsilon_z$ ). When the nominal compressive strain reaches 75%, there is only about 5% material particles with positive  $\epsilon_z$ .

## 9 Conclusions

In this investigation, the MPM method was used to simulate the response of BMG foam ( $\text{Pd}_{43}\text{Ni}_{10}\text{Cu}_{27}\text{P}_{20}$ ) under compression. The complex internal structure of the foam was modeled using material points in 3D, based on spatial density from micro-tomography. Background grid sizes were evaluated and it was found that when the grid size is the same as the voxel size, high simulation accuracy is achieved.

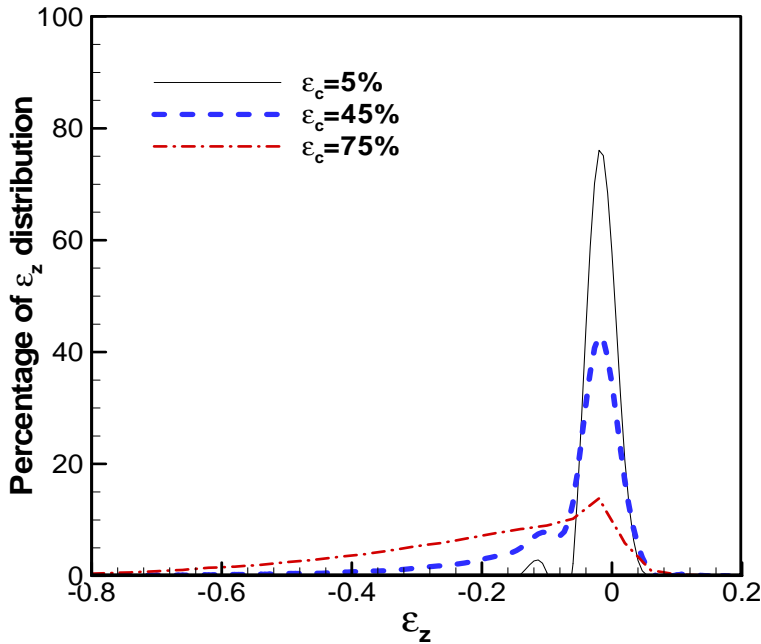


Figure 21: Histograms of  $\epsilon_z$  at different nominal compressive strains  $\epsilon_c$  at location 2.

Volume elements at two locations in the foam sample were taken for simulation of compression to compare with the results of the experiments. Numerical tests showed that linear interpolation between the Young's modulus of each material point and the grayscale of each voxel is appropriate for the simulation. It was found that the size of the volume element as well as the porosity of the corresponding volume element can affect the simulated stress-strain curve of the foam. The minimum size of the representative volume element (RVE) was determined by matching the simulated stress-strain curve with the experimental data. At the location containing the macroscopic failure plane, the minimum RVE size is 120 voxels (7.5 average cell diameters) in each direction. At another location, without the macroscopic failure plane, the RVE can be as small as 60 voxels (2.8 average cell diameters) in each direction.

A shear failure model, based on the equivalent plastic strain, was used to simulate incipient failure in the foam and failed material points were deleted from the simulation. When an appropriate failure strain is used, the first incipient slip in the foam can be correctly predicted in the simulation. Simulations of full compression of two RVE's were also conducted to investigate compaction by assuming a ductile

matrix. Results indicate that densification of the foam starts at 35% compressive strain, which is indicated by the gradual increase of stress and completes at 70% compressive strain. The maximum shear stress on the foam walls is consistent with the experimental observations of an incipient shear band formation. The simulation approach presented in this paper can be used to effectively simulate a variety of foam materials under different loading conditions, such as tension, shear, and impact to predict the material behavior under different loading conditions.

**Acknowledgement:** This work was initially supported by a grant from the Air Force Office of Scientific Research (AFOSR) through a DEPSCoR grant (No. F49620-03-1-0281). The support from DOE Nuclear Energy University Program (NEUP) grant number 09-416 allowed the completion of the work. The authors would like to thank Dr. Craig S. Hartley, Dr. Jaimie Tiley Jr., and Dr. Brett Conner, Program Managers for the Metallic Materials Program at AFOSR for the support of this work. Thanks are also due to Dr. Richard Hornung and Dr. Andy Wissink of the Lawrence Livermore National Lab for providing the code and assistance with the use of SAMRAI. The amorphous material and tomography data used in this investigation was supplied by Dr. W. L. Johnson's group at the California Institute of Technology in collaboration with Dr. E. Ustundag's group at Iowa State University. The authors would like to acknowledge valuable discussions with Dr. M. D. Demetrio and Dr. C. Veazey and useful input from N. B. Phelps. H. Lu acknowledges the support of NSF CMMI-1031829, CMMI-1132174, and CMMI-1132175.

## References

- ABAQUS Inc.**, (2005): ABAQUS Documentation, version 6.5.
- Ashby, M. F., Evans, A., Fleck, N. A., Gibson, L. J., Hutchinson, J. W., Wadley, H. N. G.**, (2000): Metal Foams : A Design Guide. Butterworth-Heinemann, 26.
- Bardenhagen, S.G., Brydon, A.D., Guilkey, J.E.**, (2005): Insight into the physics of foam densification via numerical simulation. *Journal of the Mechanics and Physics of Solids* 53 (3), 597-617.
- Bardenhagen, S.G., Kober, E.M.**, (2004): The generalized interpolation material point method. *CMES: Computer Modeling in Engineering & Sciences* 5 (6), 477-496.
- Bardenhagen, S.G., Nairn, J.A., Lu, H.**, (2011): Simulation of Dynamic Fracture with the Material Point Method Using a Mixed J-Integral and Cohesive Law Approach, *International Journal of Fracture*, 170, 49-66.
- Brothers, A.H., Dunand, D.C.**, (2005): Ductile bulk metallic glass foams. *Advanced Materials* 17 (4), 484-486.

- Brothers, A.H., Dunand, D.C.,** (2006): Amorphous metal foams. *Scripta Materialia* 54, 513-520.
- Brown, K., Attaway, S., Plimpton, S., Hendrickson, B.,** (2000): Parallel strategies for crash and impact simulations. *Computer Methods in Applied Mechanics and Engineering* 184, 375-390.
- Brydon, A.D., Bardenhagen, S.G., Miller, E.A., Seidler, G.T.,** (2005): Simulation of the densification of real open-celled foam microstructures. *Journal of the Mechanics and Physics of Solids* 53 (12), 2638-2660.
- Conner, R.D., Johnson, W.L., Paton, N.E., Nix, W.D.,** (2003): Shear bands and cracking of metallic glass plates in bending. *Journal of Applied Physics* 94 (2), 904-911.
- Conner a, R.D., Li, Y. Nix, W.D., Johnson, W.L.,** (2004): Shear band spacing under bending of Zr-based metallic glass plates. *Acta Materialia* 52, 2429-2434.
- Demetriou, M.D., Veazey, C., Schroers, J., Hanan J. C., Johnson W. L.,** (2006): Expansion evolution during foaming of amorphous metals, *Materials Science and Engineering: A*, 448-451, 863-867.
- Demetriou, M. D., Veazey, C., Schroers, J, Hanan, J. C., Johnson, W. L.,** (2007): Thermo-plastic expansion of amorphous metallic foam. *Journal of Alloys and Compounds*, 434-435, 92-96.
- Demetriou, M.D., Hanan, J.D., Veazey, C., Michiel M.D., Lenoir, N., Ustundag, E., Johnson, W.L.,** (2007): Yielding of metallic glass foam by percolation of an elastic buckling instability. *Advanced Materials* (in press).
- Gibson, L.J., Ashby, M.F.,** (1997): *Cellular Solids: Structure and Properties*, 2nd edition. Cambridge University Press.
- Gong, L., Kyriakides, S., Jang, W.Y.,** (2005): Compressive response of open-cell foams. Part I: Morphology and elastic responses, *Int. Journal of Solids and Structures* 42, 1355-1379.
- Gong, L., Kyriakides, S.,** (2005): Compressive response of open-cell foams. Part II: Initiation and spreading of crushing, *Int. Journal of Solids and Structures* 42, 1381-1399.
- Gong, L., Kyriakides, S., Triantafyllidis, N.,** (2005): On the stability of Kelvin cell foams under compressive loads, *Journal of the Mechanics and Physics of Solids* 53, 771-794.
- Hanan, J.C., Demetriou, M.D., Veazey, C., DeCarlo, F., Thompson, S.,** (2005): 1. Microtomography of amorphous metal during thermo-plastic foaming. *Advances in X-Ray Analysis* 49, 85-91.
- Hanan, J.C., Johnson, W.L., Peker, A.,** (2005): 2, NASA NTR-41102.

**Hoffmann, D. C., Suh, J.-Y., Wiest, A., Duan G., Lind, M.-L., Demetriou, M. D., Johnson, W. L.,** (2008): Designing metallic glass matrix composites with high toughness and tensile ductility. *Nature* 451, 1085-1089.

**Jones, R.M.,** (1999): *Mechanics of Composite Materials*, 2nd ed. Taylor & Francis.

**Katti, A., Nilesh, S., Samit, R., Lu, H., Fabrizio, E.F., Dass, A., Capadona, L.A., Leventis, N.,** (2006): Chemical, physical, and mechanical characterization of isocyanate cross-linked amine-modified silica aerogels. *Chemistry of Materials* 18 (2), 285-296.

**Kadar, Cs., Maire, E., Borbely, A., Peix, G., Lendvai, J., Rajkovits, Zs.,** (2004): X-Ray tomography and finite element simulation of the indentation behavior of metal foams. *Materials Science and Engineering A* 387-389, 321-325.

**Kumar, G, Desai, A., Schroers, J.,** (2010): Bulk Metallic Glass: The Smaller the Better. *Advanced Materials*, 23, 461-476.

**Luo, H., Bhat, A., Demetriou, M.D., Lu, H., Hanan, J.C.,** (2009): Dynamic Compressive Behavior of Bulk Metallic Glass Foam. High Speed Full-field Optical Measurements I SEM Annual Conference & Exposition on Experimental and Applied Mechanics 392.

**Ma, J., Lu, H., Wang, B., Roy, S., Hornung, R., Wissink, A., Komanduri, R.,** (2005): Multiscale simulations using generalized interpolation material point (GIMP) method and SAMRAI parallel processing. *CMES: Computer Modeling in Engineering & Sciences* 8 (2), 135-152.

**Ma, J., Lu, H., Komanduri, R.,** (2006): Structured mesh refinement in generalized interpolation material point (GIMP) method for simulation of dynamic problems. *CMES: Computer Modeling in Engineering & Sciences*, 12, No.3, 213-227.

**Meguid, S.A., Heyerman, J., Stranart, J.C.,** (2002): Finite element modeling of the axial collapse of foam-filled structures. *Journal of Spacecraft and Rockets* 39 (6), 828-832.

**Meguid, S.A., Stranart, J.C., Heyerman, J.,** (2004): On the layered micromechanical three-dimensional finite element modeling of foam-filled columns. *Finite Elements in Analysis and Design* 40, 1035-1057.

**Miller, R. E.,** (2000): A continuum plasticity model for the constitutive and indentation behaviour of foamed metals. *International Journal of Mechanical Sciences* 42, 729-754.

**Schroers, J., Veazey, C., Johnson, W.L.,** (2003): Amorphous metallic foam. *Applied Physics Letters* 82 (3), 370-372.

**Sulsky, D., Zhou, S.J., Schreyer, H.L.,** (1995): Application of a particle-in-cell

method to solid mechanics. *Computer Physics Communications* 87, 236-252.

**Tan, H., Nairn, J.A.,** (2002): Hierarchical, adaptive, material point method for dynamic energy release rate calculations. *Computer Methods in Applied Mechanics and Engineering* 191, 2095-2109.

**Veazey, C., Demetriou, M. D., Schroers, J., Hanan, J. C., Dunning, L. A., Kaukler, W. F., Johnson, W. L.,** (2006): Foaming of Amorphous Metals Approaches the Limit of Microgravity Foaming. *Advanced Materials and Processes* (in press).

**Wada, T., Inoue, A.,** (2003): Fabrication, thermal stability and mechanical properties of porous bulk glassy Pd-Cu-Ni-P alloys. *Materials Transactions* 44 (10), 2228-2231.

**Wada, T., Inoue, A., Greer, A.L.,** (2005): Enhancement of room-temperature plasticity in a bulk metallic glass by finely dispersed porosity. *Applied Physics Letters* 86 (25), 251907.

**Wada, T., Inoue, A.,** (2007): Production of bulk glassy alloy foams by high pressure hydrogen. *Materials Science and Engineering A* (447) 254–260.

**Wang, B., Karuppiyah, V., Lu, H., Roy, S., Komanduri, R.,** (2005): Two-dimensional mixed mode crack simulation using the material point method. *Mechanics of Advanced Materials and Structures* 12 (6), 471-484.

**Wang, Y., Cuitino, A.M.,** (2000): Three-dimensional nonlinear open-cell foams with large deformations. *Journal of the Mechanics and Physics of Solids* 48 (5), 961-988.

**Wicklein, M., Thoma, K., Vincenzini, P., Lami, A. (Eds.),** (2004): Computational Modelling and Simulation of Materials III, Part A. Techna Group, Faenza, 717–723.

**Wicklein, M., Thoma, K.,** (2005): Numerical investigations of the elastic and plastic behavior of an open-cell aluminum foam. *Materials Science and Engineering A* 397, 391-399.

**Zhu, H.X., Mills, N.J., Knott, J.F.,** (1997): Analysis of the high strain compression of open-cell foams. *J Mechanics and Physics of Solids* 45 (11/12), 1875-1904.